Adjoint Tomography of Northeast Japan Revealed by Common-Source Double-Difference Travel-Time Data

Jing Chen†1, Guoxu Chen†2, Hao Wu2, Jiayuan Yao1, and Ping Tong*1

Abstract

We present the wave equation-based adjoint tomography of northeastern Japan using common-source double-difference travel-time data. More than 30,000 high-quality first *P*-wave arrivals from 117 local earthquakes recorded by 713 seismic stations are included in the inversion, generating more than 350,000 double-difference travel times of first *P*-wave arrivals. In comparison with commonly used travel-time data, the common-source double-difference travel times are insensitive to source parameters and source-side structures but place enhanced constraints on receiver-side structures. As a result, these robust double-difference travel times generate a reliable V_P model down to a depth of 120 km. Our inversion results clearly show crustal low-velocity anomalies beneath the volcanic arc. The subducting Pacific slab is illuminated as a landward-dipping high-velocity anomaly, and the arc magmatism in the mantle wedge is shown as low-velocity anomalies. Thanks to the newly operated Seafloor Observation Network (S-net), prominent high-velocity bodies are detected in the fore-arc mantle wedge at depths of 30–60 km. These abnormal high-V_P bodies indicate a low degree of serpentinization in the fore-arc mantle wedge at low temperatures, correlating well with the previous finding that the uppermost mantle in the Kuril and Tohoku fore-arc is cold and dry. Our inversion results reveal reliable tectonic features in the subduction zone beneath northeastern Japan, suggesting that wave equation-based common-source double-difference travel-time adjoint tomography is an effective and robust method to illuminate detailed structures of the crust and uppermost mantle.

Cite this article as Chen, J., G. Chen, H. Wu, J. Yao, and P. Tong (2022). Adjoint Tomography of Northeast Japan Revealed by Common-Source Double-Difference Travel-Time Data, *Seismol. Res. Lett.* **XX**, 1–17, doi: 10.1785/0220210317.

Supplemental Material

Introduction

Seismic tomography is a powerful technique to illuminate the Earth's interior. In theory, approximate relationships between the model parameter $\boldsymbol{m}$ and theoretical prediction $\boldsymbol{G}(\boldsymbol{m})$ can be established based on reasonable physical–mathematical models (Rawlinson *et al.*, 2010), for example, by assuming that seismic-wave propagation satisfies eikonal equations or wave equations. In general, the goal of seismic tomography is to determine an appropriate model parameter $\boldsymbol{m}$ so that theoretical predictions $\boldsymbol{G}(\boldsymbol{m})$ can fit seismic observations $\boldsymbol{d}_{\text{obs}}$.

Seismic tomography involves two key ingredients: the forward modeling of wave propagation, and the misfit between observed and synthetic signals. First, most seismic tomography methods in the early stage were based on ray theory because of its simplicity and the limitation of computing power (e.g., Aki and Lee, 1976; Thurber, 1983; Kissling, 1988; van der Hilst *et al.*, 1997). This high-frequency assumption indeed reduces the total computing cost, whereas it ignores finite-frequency effects such as wavefront healing and scattering (Marquering *et al.*, 1999; Dahlen *et al.*, 2000; Hung *et al.*, 2001). The ignorance of finite-frequency effects may lose resolution in resolving small-scale anomalies (Yoshizawa and Kennett, 2004; Zhou *et al.*, 2005). With the rapid development of computing power and numerical algorithms in the past few decades, it is becoming more popular to simulate wave propagation by directly solving wave equations. This approach avoids the infinite-frequency assumption of ray theory and takes finite-frequency effects into account. Thus, it is possible to obtain accurate and high-resolution inversion results, making waveform inversion a promising method for seismic tomography (e.g., Bamberger *et al.*, 1982; Igel *et al.*, 1996; Pratt, 1999; Tromp *et al.*, 2005; Fichtner *et al.*, 2006; Chen *et al.*, 2007; Tape *et al.*, 2009).

---

1. School of Physical and Mathematical Sciences, Nanyang Technological University, Singapore, Singapore, https://orcid.org/0000-0002-9083-3940 (JC); https://orcid.org/0000-0002-1937-3427 (PT); 2. Department of Mathematical Sciences, Tsinghua University, Beijing, China

*Corresponding author: tongping@ntu.edu.sg

†These authors contributed equally to this work.

Second, an appropriate misfit between observed and synthetic signals sensitive to the model parameter $\boldsymbol{m}$ of our interest but less affected by other factors should be designed. Traditionally, the model parameter $\boldsymbol{m}$ is updated by minimizing the mismatch between the observed data $\boldsymbol{d}_{\mathrm{obs}}$ and theoretical prediction $\boldsymbol{G}(\boldsymbol{m})$, which arises from not only the inconsistency of the model parameter $\boldsymbol{m}$, the noise in the observed seismograms, but also uncertainties of the source term, including the source time function, the source mechanism, the earthquake location, and the origin time (Tape *et al.*, 2010). Thus, uncertainties of the source term may introduce artificial anomalies to the final model, resulting in inaccurate tomographic results. To mitigate this influence, a new wave equation-based adjoint tomography method using common-source double-difference travel-time data was proposed (de Vos *et al.*, 2013; Yuan *et al.*, 2016), which measures the discrepancy between observations and simulations in terms of the cross-correlation travel-time difference made on station pairs. This new measurement has been proved invariant to seismic moment and the origin time shift and insensitive to earthquake source wavelet, making this double-difference travel-time tomography method a robust technique to determine the Earth's internal structure (Yuan *et al.*, 2016; Örsvuran *et al.*, 2020). In addition, common-source double-difference travel time is less affected by source-side structure, because it efficiently suppresses the influence arising from the anomaly surrounding the earthquake. Notably, even one earthquake could resolve significant structural details, making it possible to obtain high-resolution results with a limited number of earthquakes (Yuan *et al.*, 2016).

The idea of differential measurement could date back to the 1960s (Brune and Dorman, 1963). Its extended concept, called "double-difference," was then introduced to locate earthquakes (Poupinet *et al.*, 1984; Fremont and Malone, 1987; Got *et al.*, 1994) and initiated the development of the software package "hypoDD" for precisely locating earthquakes (Waldhauser and Ellsworth, 2000). Furthermore, "tomoDD" was developed to simultaneously obtain earthquake locations and velocity structures (Zhang and Thurber, 2003). Afterward, accurate earthquake locations and robust tomographic results were obtained using double-difference travel-time measurements, promoting our knowledge of the Earth's internal structure and its evolution (e.g., Zhang *et al.*, 2004; Hirose *et al.*, 2008; Fang and Zhang, 2014; Sippl *et al.*, 2018). However, most studies are based on seismic ray theory but rarely perform double-difference travel-time inversions by solving wave equations. de Vos *et al.* (2013) derive the finite-frequency sensitivity kernel for two-station surface-wave measurements. The properties of sensitivity kernels for the group velocity and phase velocity are discussed in detail. Double-difference travel-time measurements are then inverted to build subsurface velocity models (Yuan *et al.*, 2016; Örsvuran *et al.*, 2020). These studies exhibit complete theoretical analyses and ideal numerical experiments, however, requiring real data inversion to verify the effectiveness of this new method. In this article, following the scheme proposed by Yuan *et al.* (2016), we perform the wave equation-based adjoint tomography by inverting common-source double-difference travel-time data in northeastern Japan.

Strong seismic and volcanic activities occur in Japan, where four lithospheric plates exist with intense interactions (Fig. 1). In our study region of northeastern Japan, the Pacific plate is subducting northwestward from the Kuril–Japan trench and beneath the Okhotsk plate at a rate of 7–10 cm/yr (Bird, 2003; Zhao, 2015). The water is dragged into the mantle by the oceanic subducting slab and then released to the mantle wedge, triggering arc magmatism and partial melting in the mantle wedge. Unlike warm subduction zones such as southwestern Japan, where the Philippine Sea plate is subducting northwestward from the Nankai trough at a rate of 4–5 cm/yr (Zhao, 2015), the subduction zone in northeast Japan is relatively cold. It causes the hydrous minerals to break down in the uppermost mantle at a deeper depth of ~70 km (Furukawa, 1993), leading to a dry fore-arc mantle wedge. These features make northeast Japan a natural laboratory to study the subduction process. Importantly, the dense seismic stations deployed on the islands and recently on the adjacent oceanic bottom provide abundant data to evaluate the effectiveness of the wave equation-based adjoint tomography method using common-source double-difference travel-time data.

The rest of this article is organized as follows. We begin with a brief introduction to the seismograms and the procedures to obtain differential travel times via cross-correlation techniques in the Data section. Then, we present the inversion method in the Inversion method section. The Results section illustrates the tomographic results derived from real data, in which the resolution and the robustness of anomalies are analyzed with the checkerboard and restoring resolution tests. Following that, some discussions are presented in the Discussion section to explain the anomalies revealed in the tomographic images. Finally, we conclude this article in the Conclusion.

Data

Our study region is composed of Honshu and Hokkaido islands together with surrounding oceanic areas, ranging from 34° E to 46° E in latitude and 135° W to 146° W in longitude. Figure 2a shows 713 permanent seismic stations distributed uniformly and densely in the study region, among which 566 stations belong to the Hi-net network (Okada *et al.*, 2004) and 147 stations belong to the S-net network (Kanazawa, 2013; Takagi *et al.*, 2019). Hi-net is a high-sensitivity seismograph network deployed on the Japan Islands (Fig. 2a, red squares). It has a station interval of about 30 km in Honshu and Hokkaido, providing sufficient constraints on the

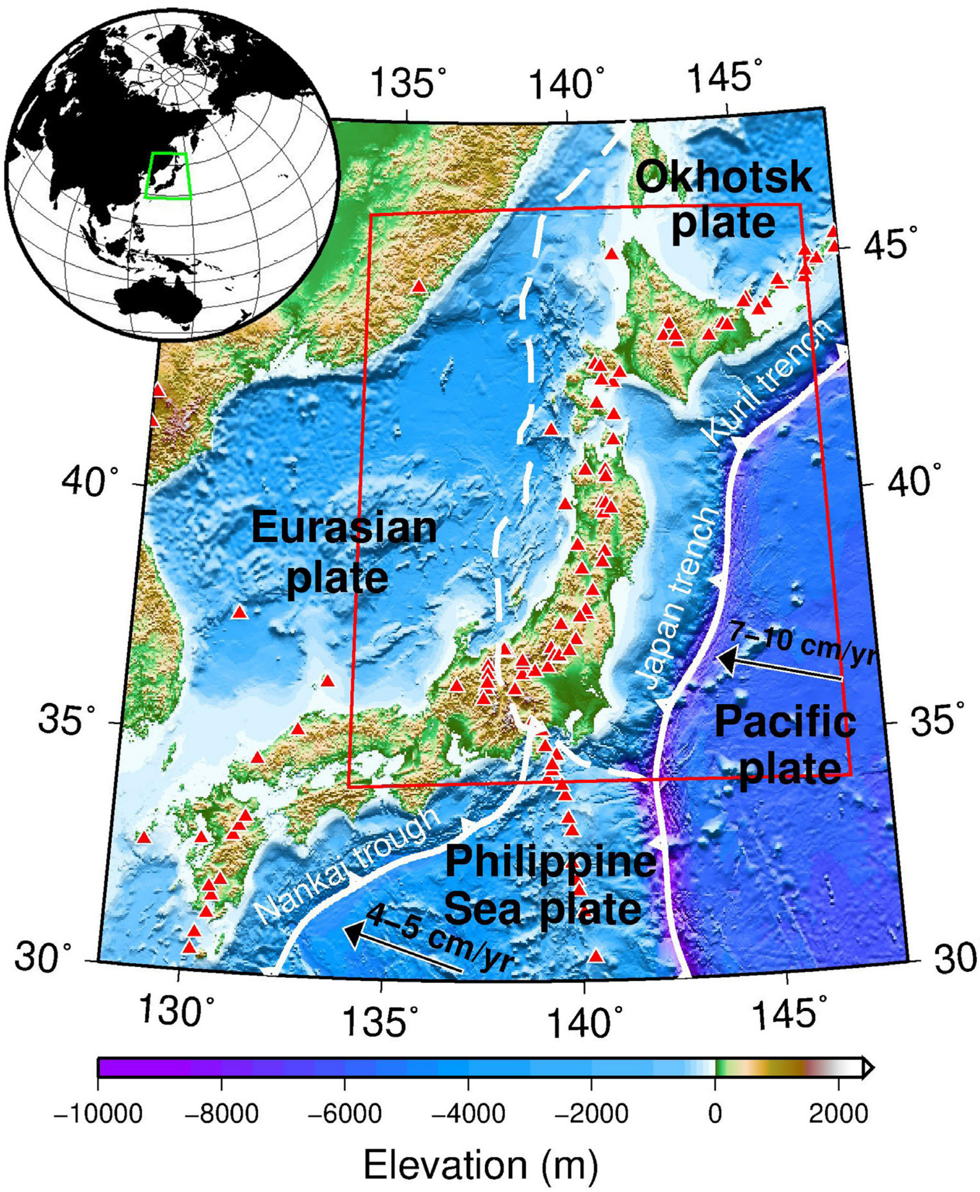

Figure 1. Illustration of the Japan Islands. Our study region within the red box consists of Hokkaido, Honshu, and adjacent oceanic regions. The red triangles denote main volcanoes. The white solid lines (boundary of subduction zone) and dashed lines (continental or oceanic convergent boundary) indicate the tectonic boundaries of labeled plates (Bird, 2003). In the northeast, the Pacific plate is subducting northwestward beneath the Okhotsk plate from the Kuril–Japan trench at a rate of 7–10 cm/yr. In the southwest, the Philippine Sea plate is subducting northwestward from the Nankai trough at a rate of 4–5 cm/yr. The box in the upper left inset map shows the location of the Japan Islands. The color version of this figure is available only in the electronic edition.

subsurface structure beneath the northeastern Japan Islands. In addition to these land-based seismic stations, seismic data recorded by S-net are also taken into account to enhance the data coverage in the surrounding ocean (Fig. 2a, blue squares). These permanent ocean-bottom seismometers have a station interval of about 30 km in the east–west direction and about 50–60 km in the north–south direction, which are slightly sparser than the Hi-net.

We carefully select earthquakes for the inversion to balance computational cost and data coverage. The study region is divided into many cubic blocks with a size of $1^\circ \times 1^\circ \times 10$ km in latitude, longitude, and depth, within which earthquakes are selected depending on the number of useful recordings and magnitude. Finally, 117 earthquakes from 2004 to 2019 with magnitude ranging from 4.5 to 7.0 are included in the inversion (Fig. 2b, colorful circles). The final data set consists of 38,566 useful three-component waveforms. These waveforms have a dense data coverage in the study region, providing sufficient constraints on the crust and the uppermost mantle in the fore-arc and volcanic arc region beneath northeast Japan.

A series of procedures are required to process the raw data to obtain differential travel times. A differential travel time is the travel-time difference of seismic waves originating from the same earthquake but arriving at two separated stations. First, we use the software Seismic Analysis Code (SAC) to remove the instrument response and filter the observed seismic signals, generating processed waveforms in the period band of 5–10 s (Goldstein and Snoke, 2005). Then, the theoretical first *P*-arrival times are calculated based on the average local 1D model from Simutė *et al.* (2016) by software SIMULPS12 (Thurber, 1983; Evans *et al.*, 1994; Chen *et al.*, 2020), according to which adapted time windows are determined to extract first *P*-wave arrivals (Fig. 3). The time windows ranging from 20 s before to 15 s after the first *P*-arrival are initially selected, and then manually checked and adjusted when needed. Finally, the processed signals are used to calculate the differential travel time $\Delta t^{\mathrm{obs}}_{ij,k}$ from one common source (k) to a station pair (i and j) via the cross-correlation technique, defined as:

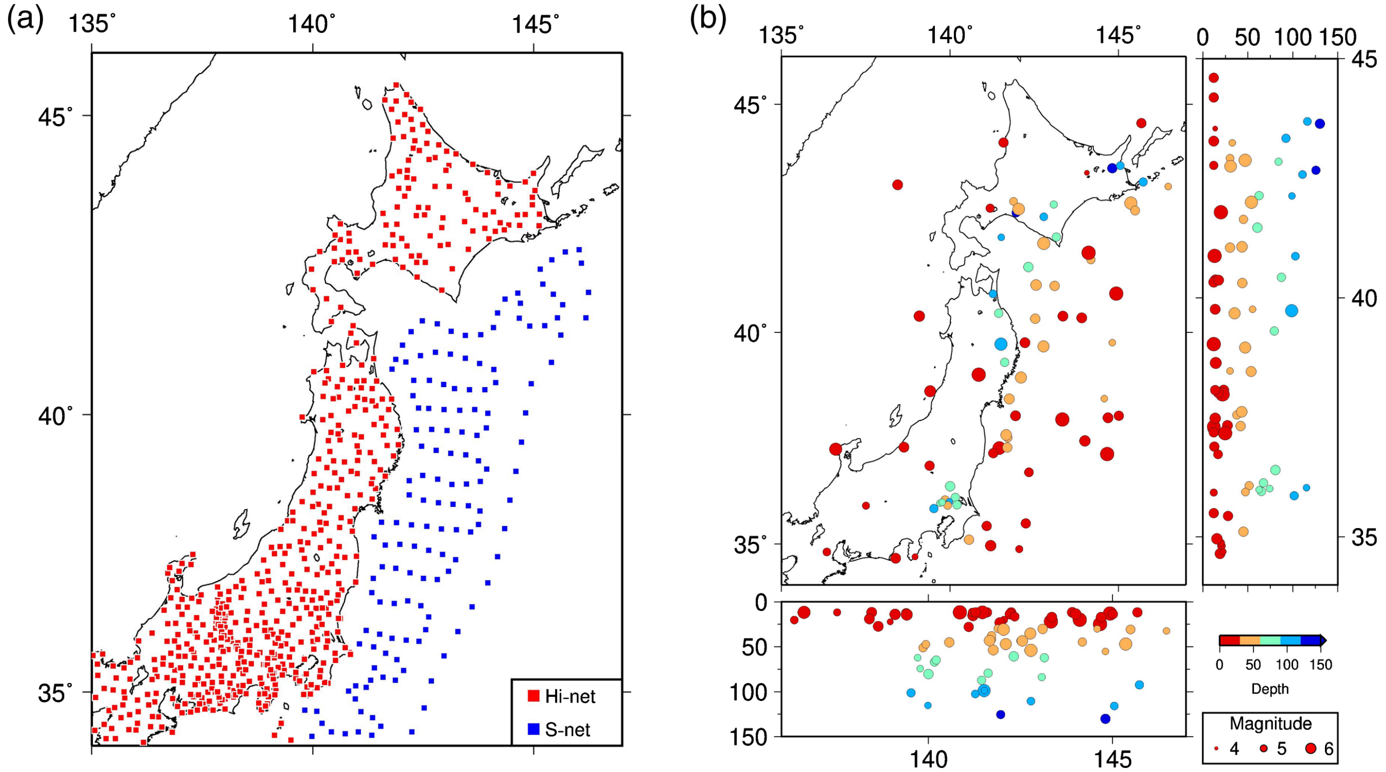

Figure 2. Illustration of the earthquakes and stations included in the data set. (a) About 713 seismic stations are included in the inversion, among which 566 stations in red belong to High Sensitivity Seismograph Network (Hi-net), and the rest in blue are oceanic-bottom stations of Seafloor Observation Network (S-net). (b) The inversion involves 117 earthquakes uniformly distributed in the study region, which are denoted as circles. The size and color indicate magnitude and depth, respectively. The color version of this figure is available only in the electronic edition.

$$\Delta t^{\mathrm{obs}}_{ij,k} = \arg\max_{\tau} \int_0^T d_{i,k}(t+\tau)\, d_{j,k}(t)\,\mathrm{d}t. \tag{1}$$

Here $d_{i,k}(t)$ and $d_{j,k}(t)$ indicate the processed signals recorded at two separated stations. Figure 4 exhibits the cross correlation of some processed observed signals used in the inversion, illustrating a high level of similarity in paired signals and robust cross-correlation travel-time differences. Two ingredients guarantee the high quality of cross-correlation travel-time differences. First, strict criteria are adopted to select appropriate station pairs, which will be clarified in the Forward modeling and double-difference travel time section. Second, cross correlation is performed between observed signals instead of between observed and synthetic signals, ensuring the consistency of the source term between compared signals.

Inversion Method

We perform the wave equation-based adjoint tomography to derive the 3D V_P model beneath northeast Japan and adjacent oceanic regions using the common-source double-difference travel times extracted from first P-wave arrivals. Further details regarding forward modeling, double-difference travel time, sensitivity kernel, initial model, and optimization algorithm are described in the following sections.

Forward modeling and double-difference travel time

We apply the spectral element method to simulate seismic-wave propagation to obtain synthetic signals. This method is not only feasible in parallel computing and flexible in mesh design but also accurate in forward modeling (Komatitsch and Vilotte, 1998; Fichtner, Igel, *et al.*, 2009; Gokhberg and Fichtner, 2016). The spectral element method combines the advantages of the pseudospectral method and the finite-element method, making it a wildly used numerical algorithm in seismological research (e.g., Fichtner, Kennett, *et al.*, 2009; Tape *et al.*, 2010; Simutė *et al.*, 2016). In this work, we employ the graphic processing units accelerated SPECFEM3D globe program package to calculate synthetic signals and sensitivity kernels (Komatitsch and Tromp, 1999; Komatitsch, 2011). There are 127,100 spectral elements consisting of 8.4×10^7 Gauss-Lobatto-Legendre (GLL) grid points in the study region, with an average grid spacing of 4.5 km. The minimum P-wave wavelength that can be resolved by SPECFEM3D is about 50 km, corresponding to a period of about 7.8 s. The undulating topography and the Moho interface from CRUST1.0 (Laske *et al.*, 2013) are taken into account in the meshing process. The absolute V_P and other model parameters are discretized on these grid points, describing the subsurface structure beneath

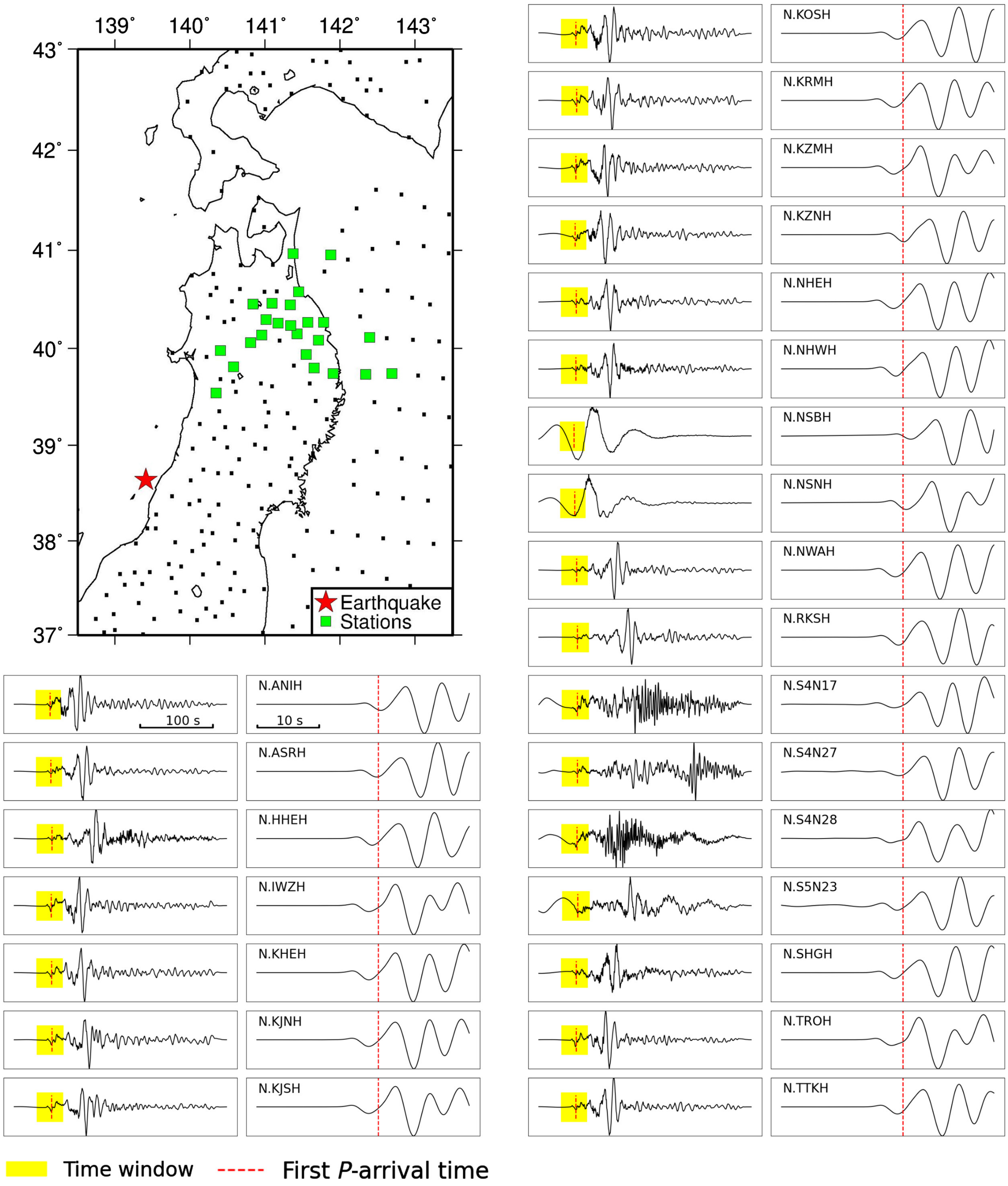

Figure 3. Illustration of data preprocessing. The earthquake (red star) and stations (green squares) are plotted in the upper left figure. Raw data are aligned in the left column. After filtering and selecting time windows from 20 s before to 15 s after theoretical first *P*-wave arrival times (red dashed lines), we obtain the processed signals (right column). The color version of this figure is available only in the electronic edition.

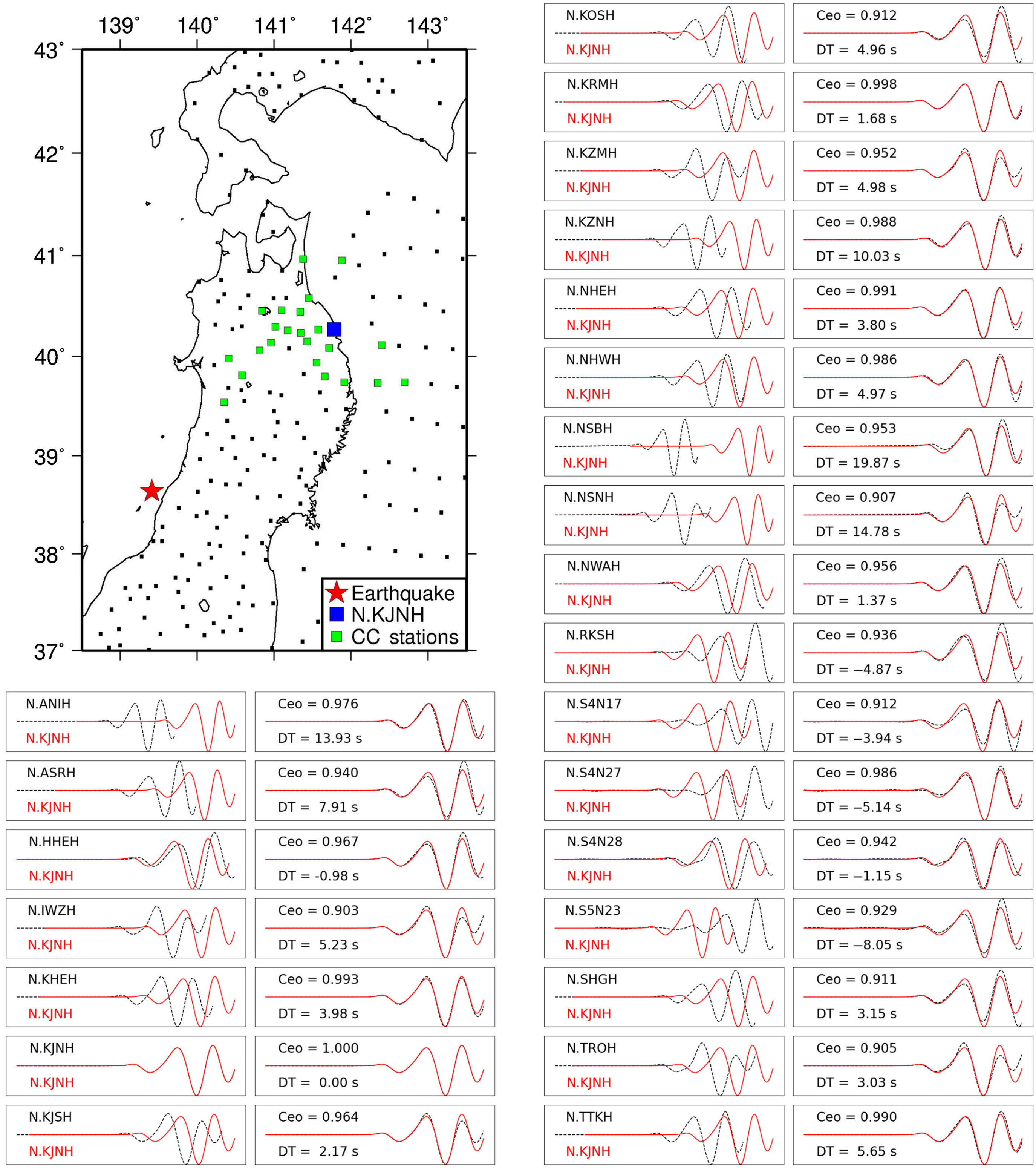

Figure 4. Illustration of cross correlations of recorded signals. The earthquake (red star) and stations (squares) are plotted in the upper left figure. The blue square indicates the reference station. The green squares denote the stations that are cross correlated with the reference station. Left column: the processed signals of two separated stations. Right column: the processed signals with the time shift calculated from the cross correlation. The cross-correlation coefficient (Ceo) and the time shift (DT) are presented. The color version of this figure is available only in the electronic edition.

northeast Japan. We choose the Ricker wavelet with a dominant frequency of 8 s as the source time function. Although there exists inconsistency in the real source time function and the Ricker wavelet, it has ignorable influence on the double-difference travel time and corresponding sensitivity kernels. The cross correlation is performed between synthetic signals originating from the same earthquake and arriving at two neighboring stations. Thus, the source wavelet information is eliminated, and the differential travel time is preserved. It is also called the source wavelet invariance (see section 4.3 in Yuan *et al.*, 2016). In a similar manner as processing the observed signals, adapted time windows are applied to synthetic signals according to theoretical first *P*-wave arrival times at each iterative step.

We measure the double-difference travel time $\Delta\Delta t_{ij,k}$ calculated by further cross correlating the processed synthetic signals originating from the same earthquake (k) but arriving at two separate stations (i and j), defined as

$$\Delta\Delta t_{ij,k} = \Delta t^{\mathrm{syn}}_{ij,k} - \Delta t^{\mathrm{obs}}_{ij,k}, \tag{2}$$

in which

$$\Delta t^{\mathrm{syn}}_{ij,k} = \arg\max_{\tau} \int_0^T s_{i,k}(t+\tau) s_{j,k}(t)\mathrm{d}t. \tag{3}$$

Here $s_{i,k}(t)$ and $s_{j,k}(t)$ indicate the processed synthetic signals recorded at a station pair (i and j). And $\Delta t^{\mathrm{obs}}_{ij,k}$ is the differential travel time of observed signals calculated in equation (1). The primary goal is to obtain an appropriate V_P model to match the calculated differential travel time $\Delta t^{\mathrm{syn}}_{ij,k}$ with the observed differential travel time $\Delta t^{\mathrm{obs}}_{ij,k}$. Accordingly, we can define the objective function as

$$\chi = \sum_{k\in E}\Big(\sum_{(i,j)\in S_k} (\Delta\Delta t_{ij,k})^2\Big), \tag{4}$$

in which E is a set containing all used earthquakes, and S_k is the corresponding set consisting of possible station pairs. At each iteration step, the objective function χ is rebuilt by only involving carefully selected double-difference travel times. First of all, we only include the station pairs with similar signals for which cross-correlation coefficients are larger than 0.9 (e.g., VanDecar and Crosson, 1990; Richards-Dinger and Shearer, 2000; Yuan *et al.*, 2016). The cross-correlation coefficient directly reflects the similarity of compared signals that mainly influences the accuracy and reliability of the calculated differential travel time. Second, the epicenter distance should be comparable to the width of the first Fresnel zone, limited within the range of 50–600 km (e.g., Woodward, 1992; Baig *et al.*, 2003; Yuan *et al.*, 2016). To avoid the influence of source-side structure, the angle from the earthquake to two separated stations is within 20°, and the distance between the two stations should be smaller than 300 km. Finally, the double-difference travel times larger than 3 s are considered unreliable and thus abandoned. These strategies guarantee the accuracy and reliability of the used double-difference travel times.

Initial model

The wave equation-based inversion requires an appropriate initial model to reduce the risk of being trapped in a local minimum (Simutė *et al.*, 2016; Tromp, 2020). Otherwise, an inaccurate starting model might lead to more iteration steps or even introduce artificial anomalies to the final imaging result (Kissling *et al.*, 1994). In our study, the undulating Conrad and Moho discontinuities from CRUST1.0 (Laske *et al.*, 2013) are embedded in the 3D starting model, in which V_P is 6.0 km/s in the upper crust and 6.7 km/s in the lower crust (Zhao *et al.*, 1992). The layered ak135 model is adopted to represent the mantle structure of the starting model without assigning any perturbations to the slab (Kennett *et al.*, 1995). Finally, we smooth this 3D model to construct a smooth initial model for the inversion. Its vertical and horizontal profiles are displayed in Figure 5. The absolute V_P model is iteratively updated during the inversion.

Sensitivity kernel and iterative optimization

The adjoint state method is an efficient approach for computing the Fréchet derivative of the objective function with respect to the model parameter (e.g., Tarantola, 1984; Tromp *et al.*, 2005; Fichtner *et al.*, 2006). Mathematically, the Fréchet derivative can be expressed in a form of sensitivity kernel,

$$\delta\chi = \int K^{dd}_m(\boldsymbol{x})\delta\ln m(\boldsymbol{x})\mathrm{d}^3\boldsymbol{x}, \tag{5}$$

in which $K^{dd}_m(\boldsymbol{x})$ is the sensitivity kernel associated with the common-source double-difference travel time. Further, the sensitivity kernel can be written as the convolution of the forward wavefield with the adjoint wavefield. The adjoint wavefield is generated by an adjoint source at one or multiple seismic stations (Tromp *et al.*, 2005; Fichtner *et al.*, 2006). According to Yuan *et al.* (2016) (also see de Vos *et al.*, 2013), the adjoint source for the common-source double-difference travel time in equation (4) writes

$$\begin{aligned} f^{\dagger}_{ij,k}(\boldsymbol{x},t) = {} & \frac{\Delta\Delta t_{ij,k}}{N_{ij,k}}\partial_t s_{j,k}(T-t+\Delta t^{\mathrm{syn}}_{ij,k})\delta(\boldsymbol{x}-\boldsymbol{x}_i) \\ & -\frac{\Delta\Delta t_{ij,k}}{N_{ij,k}}\partial_t s_{i,k}(T-t-\Delta t^{\mathrm{syn}}_{ij,k})\delta(\boldsymbol{x}-\boldsymbol{x}_j), \end{aligned} \tag{6}$$

in which

$$N_{ij,k} = \int_0^T \partial_t^2 s_{i,k}(t+\Delta t^{\mathrm{syn}}_{ij,k}) s_{j,k}(t)\mathrm{d}t. \tag{7}$$

Both the forward field and the adjoint field can be calculated using the SPECFEM3D software package (see details in Tromp *et al.*, 2005 and Liu and Tromp, 2006), allowing the

(a) Horizontal profiles:

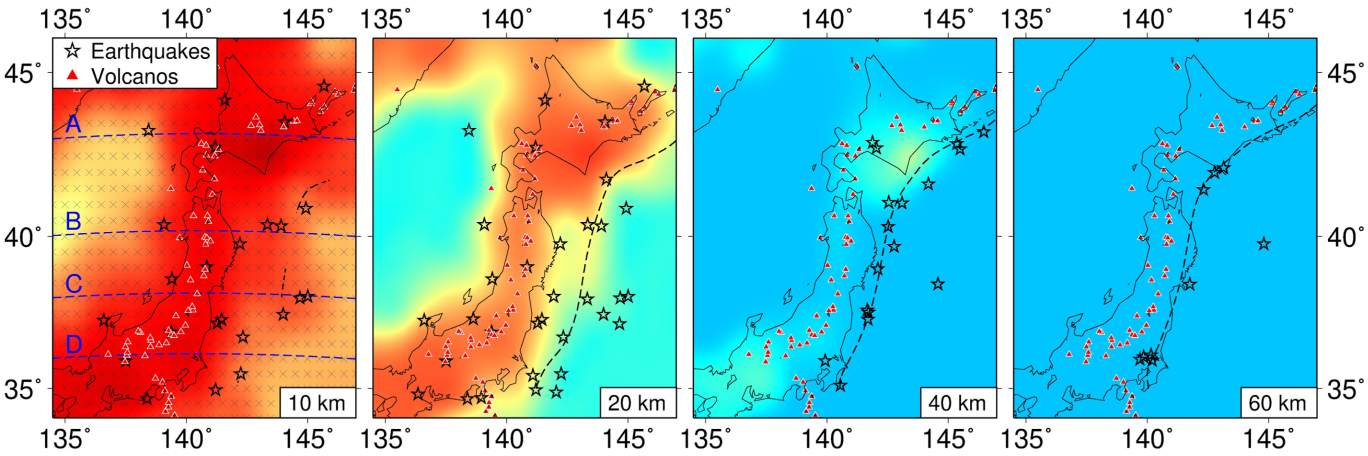

(b) Vertical profiles:

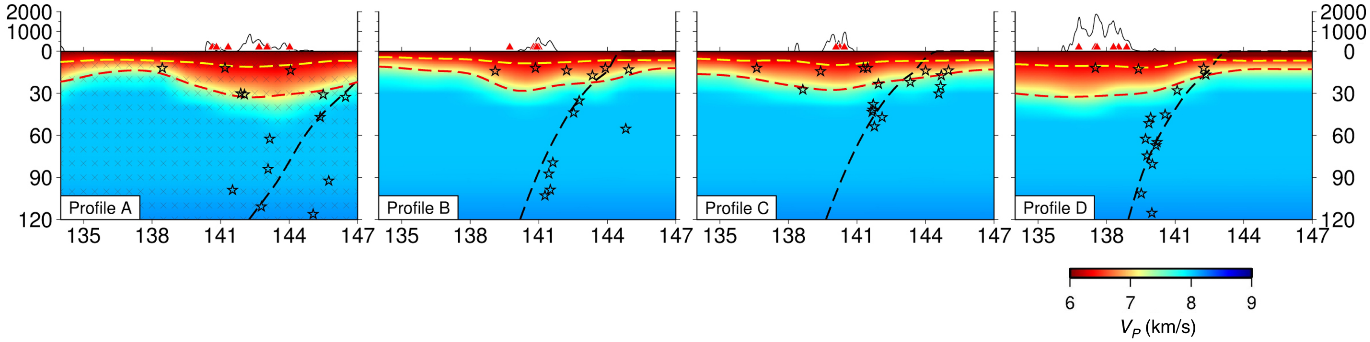

Figure 5. Illustration of the initial model. (a) The horizontal sections of the initial model at different depths. (b) The vertical profiles of the initial model along the blue dashed lines in (a) at different latitudes. The yellow and red dashed lines represent the Conrad and Moho discontinuities, respectively. The red triangles denote main volcanoes, and earthquakes used in the inversion are black stars. The black crosses represent the coarse mesh grid nodes for updating the model. The black dashed lines indicate the upper boundary of the subducting Pacific slab. The color version of this figure is available only in the electronic edition.

construction of an approximate linear relationship between the objective function χ and the model parameter $m(\boldsymbol{x})$, as shown in equation (5).

Because of the limited resolving ability of seismic data, the sensitivity kernel with respect to the P-wave velocity computed on the GLL points of the spectral elements is further projected on a coarse inversion grid with a horizontal grid spacing of 50 km and a vertical spacing of 10 km (Fig. 5, black crosses). This model parameterization has a smoothing effect on the sensitivity kernel and decreases the number of unknowns to improve the stability of the inversion. Then, a modified gradient descent method with a controlled step size is applied to update the P-wave velocity model (Tong, 2021). In the first few iterations, a limited step size of 1% for the relative P-wave velocity perturbation is preferred. With the iteration going, the step size is slightly adjusted depending on the change of the objective function. If the objective function decreases as compared to the previous step, the step size increases by 1.25 times. Otherwise, it reduces to its half. The step size is limited within 0.2%–1.5% to keep the inversion stable.

Forty iterations were performed in this study, generating a 3D V_P model beneath northeast Japan. The double-difference travel-time objective function significantly decreases by 80% (from 245,264 to 48, 889 s^2). Though the number of station pairs is slightly reduced from 425,277 to 368,381, implying that some station pairs are excluded as the cross-correlation coefficients of synthetic signals in the updated models become smaller than the threshold of 0.9. The mean value of the squared double-difference travel times is reduced by 77%. Figure 6 shows the histogram of the double-difference travel times computed in the initial and final models. It is obvious that the distribution of the double-difference travel times is more concentrated on zero after the iterative inversion. Quantitatively, the mean value of the double-difference travel times remains near zero (from −0.0042 to −0.0011 s). Moreover, the standard variance decreases from 0.7594 to 0.3643 s, implying a better fit between the synthetic and observed signals.

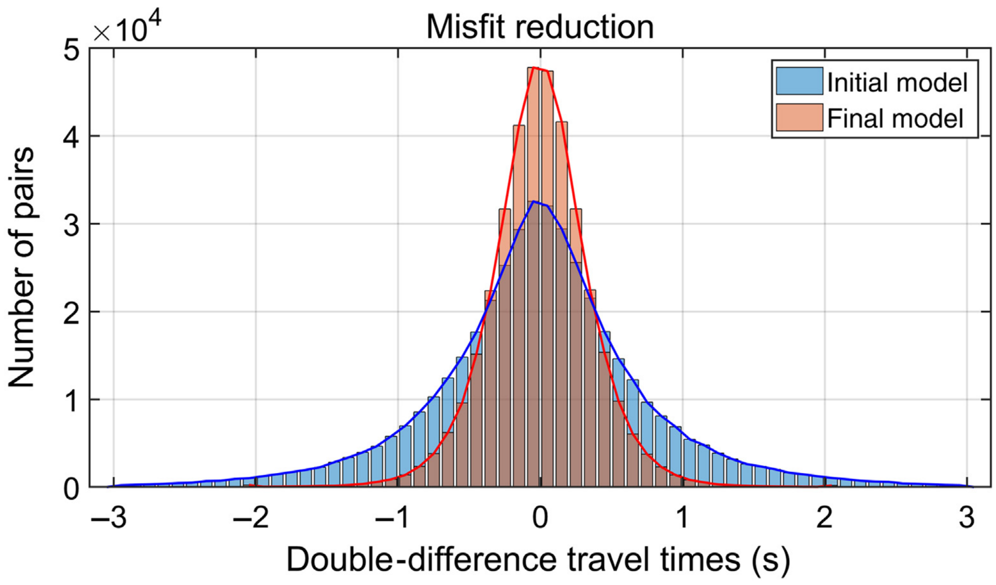

Figure 6. The histogram of double-difference travel times. The blue and red bars mean the distributions of double-difference travel times in the initial and final model, respectively. The standard variance decreases from 0.7594 to 0.3643 s, suggesting a better data fit for the output model. Meanwhile, the mean value remains near zero (from −0.0042 to −0.0011 s), suggesting that the initial and final models are reasonable. The color version of this figure is available only in the electronic edition.

Results

Tomographic images

The common-source double-difference travel-time adjoint tomography method generates a 3D V_P model of the crust and uppermost mantle down to a depth of 120 km beneath northeast Japan and surrounding oceanic regions. Horizontal sections of the absolute V_P model and the V_P perturbation model are presented in Figure 7, and vertical profiles passing through major velocity anomalies are included in Figure 8. More profiles are illustrated in Figures S1 and S2, available in the supplemental material to this article. It is noted that the V_P perturbation is calculated with respect to the 3D initial model rather than a 1D reference velocity model, which implies that the model update is purely contributed by the chosen seismic data. Thus, the perturbation model may sometimes look contrary to the absolute V_P model, especially at shallow depths where strong lateral V_P variations exist in the 3D initial model (e.g., Fig. 7, 20 km).

The horizontal sections reveal prominent low-velocity anomalies (Mb1 and Mb2) just beneath the volcanic arc (Fig. 7, 20–100 km). The low-velocity bodies extend from the crust to the uppermost mantle, sitting above the Pacific subducting slab (Mb1 in Fig. 8, profile A; Mb2 in Fig. 8, profiles B–E). In addition, the upper portion of the Pacific subducting slab is represented by the high-velocity body PAC, which well matches the upper boundary of the Pacific slab given by Slab2.0 (Hayes *et al.*, 2018) (Fig. 8, profiles B–E).

Thanks to the newly deployed S-net, several strong low- and high-velocity bodies (Mw1–Mw3, Oc1 and Oc2) are detected in the fore-arc region. The high-velocity anomaly Mw1 is located in the northeast of the study region down to a depth of 50 km (Fig. 7, 20–40 km; Fig. 8, profile A). The high-velocity bodies Mw2 and Mw3 are located east of Honshu. They are connected at shallow depths (above 20 km) but are separated in the uppermost mantle down to 50 km depth (Fig. 7, 20 and 40 km; Fig. 8, profiles B and D). By contrast, the strip-like low-velocity body, labeled by Oc1, is detected atop the subducting slab, ranging from 37° to 42° in latitude (Fig. 7, 20 and 40 km; Fig. 8, profiles B and C). In addition, a similar low-velocity anomaly Oc2 is observed in the southern termination of our study region, which disappears at a depth of 70 km (Fig. 7, 20–60 km; Fig. 8, profile E). Our tomographic result shows high consistency with previous studies (e.g., Liu and Zhao, 2016; Yu and Zhao, 2020), which supports the reliability of our result (see Figs. S3 and S4).

Checkerboard and restoring resolution tests

Even though we have carefully considered the robustness of the waveform data used in the inversion, the resolving ability of the seismic data and the reliability of the illuminated anomalies require proper evaluations, because the uneven distribution of events and stations may result in artificial anomalies in the imaging result. In this section, two types of synthetic resolution tests are designed to evaluate the resolution of tomographic images and assess the robustness of inverted anomalies for geological interpretations (e.g., Humphreys and Clayton, 1988; Zhao *et al.*, 1992).

First, the checkerboard resolution test is performed to reveal the well-resolved region. The target model is designed by alternatively assigning positive and negative V_P perturbations to the 3D initial model. From the crust to the uppermost mantle down to 200 km depth, the size of the cubic anomaly increases from $100 \times 100 \times 30$ km^3 to $300 \times 300 \times 60$ km^3, and the amplitude decreases from ±10% to ±6%. Horizontal and vertical profiles of the target V_P model passing through the centers of the anomaly blocks are illustrated in Figure 9. Besides, the output model is illustrated along the same profiles for comparison. The geometry

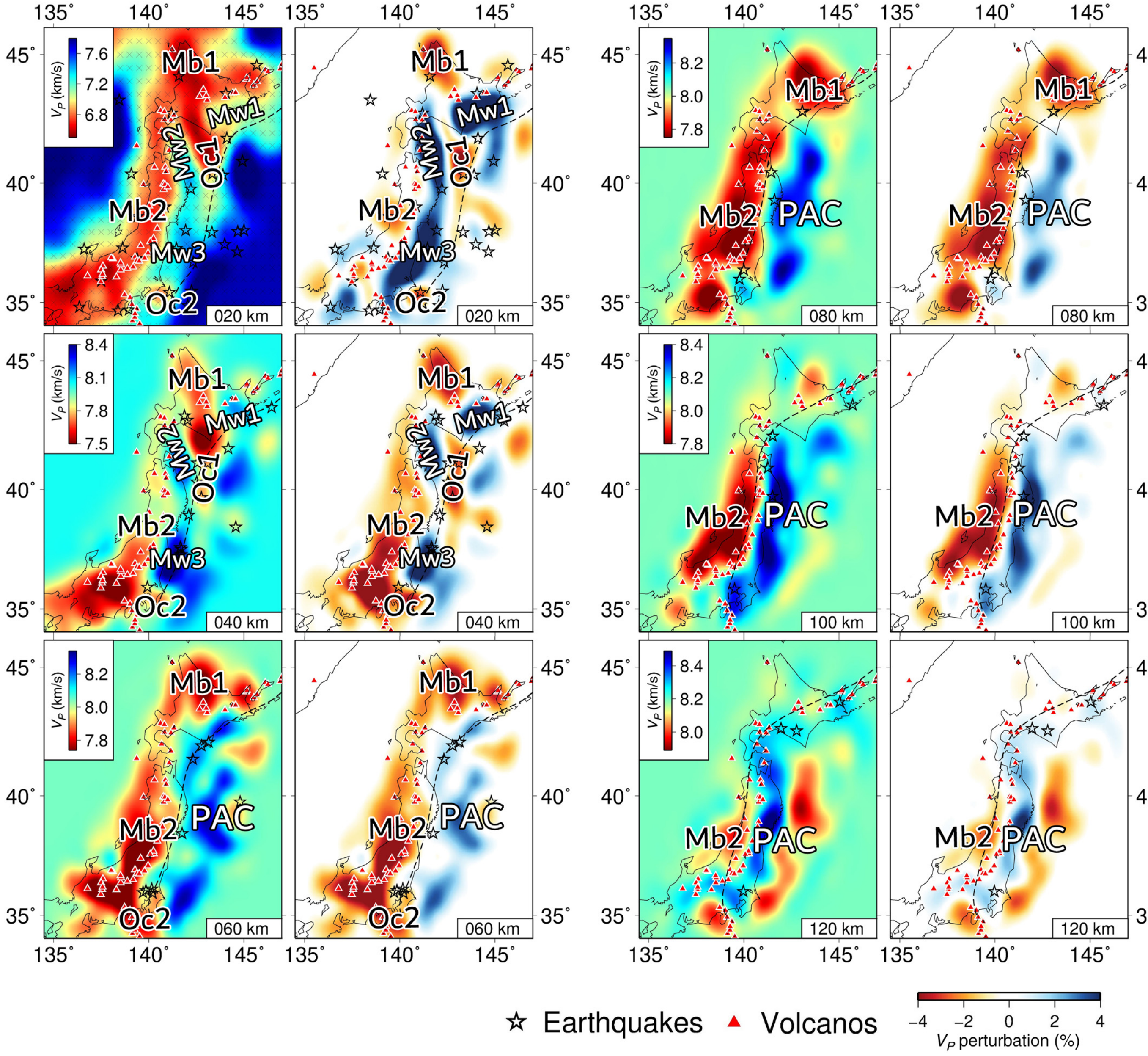

Figure 7. Horizontal profiles of the inversion result. The absolute V_P model and the V_P perturbation model with respect to the 3D initial model are presented. Prominent low- and high-velocity anomalies are labeled in each profile (PAC: the Pacific Plate; Mb1 and Mb2: magma body; Mw1–Mw3: mantle wedge; Oc1 and Oc2: oceanic crust). The stars represent the earthquakes within 20 km around the profile. The red triangles denote major volcanoes. The upper boundary of the subducting Pacific slab is denoted by black dashed lines obtained from Slab2.0 (Hayes *et al.*, 2018). The color version of this figure is available only in the electronic edition.

of positive and negative anomalies is distinguishable in the forearc and volcanic arc regions beneath the northeastern Japan Islands, where dense stations are deployed and provide sufficient data coverage. The amplitude of the recovered anomaly is smaller than the target model, which is mainly caused by the smoothing effect of the coarse inversion grid. As shown in the vertical profiles along different latitudes, the anomalies that sit above and surround the Pacific subducting slab are clearly revealed, suggesting good resolution in the subducting zone down to a depth of 120 km. This checkerboard resolution test indicates that our V_P model has a horizontal and vertical resolution of 100 and 30 km, respectively.

Second, after obtaining the tomographic result derived from real data, the restoring resolution test is performed to evaluate the robustness of illuminated structural anomalies. We design a target model that resembles the final tomographic model and execute the same procedure as the real-data inversion. Figure 10 displays the comparison between the target model and the output model, suggesting a high level of similarity

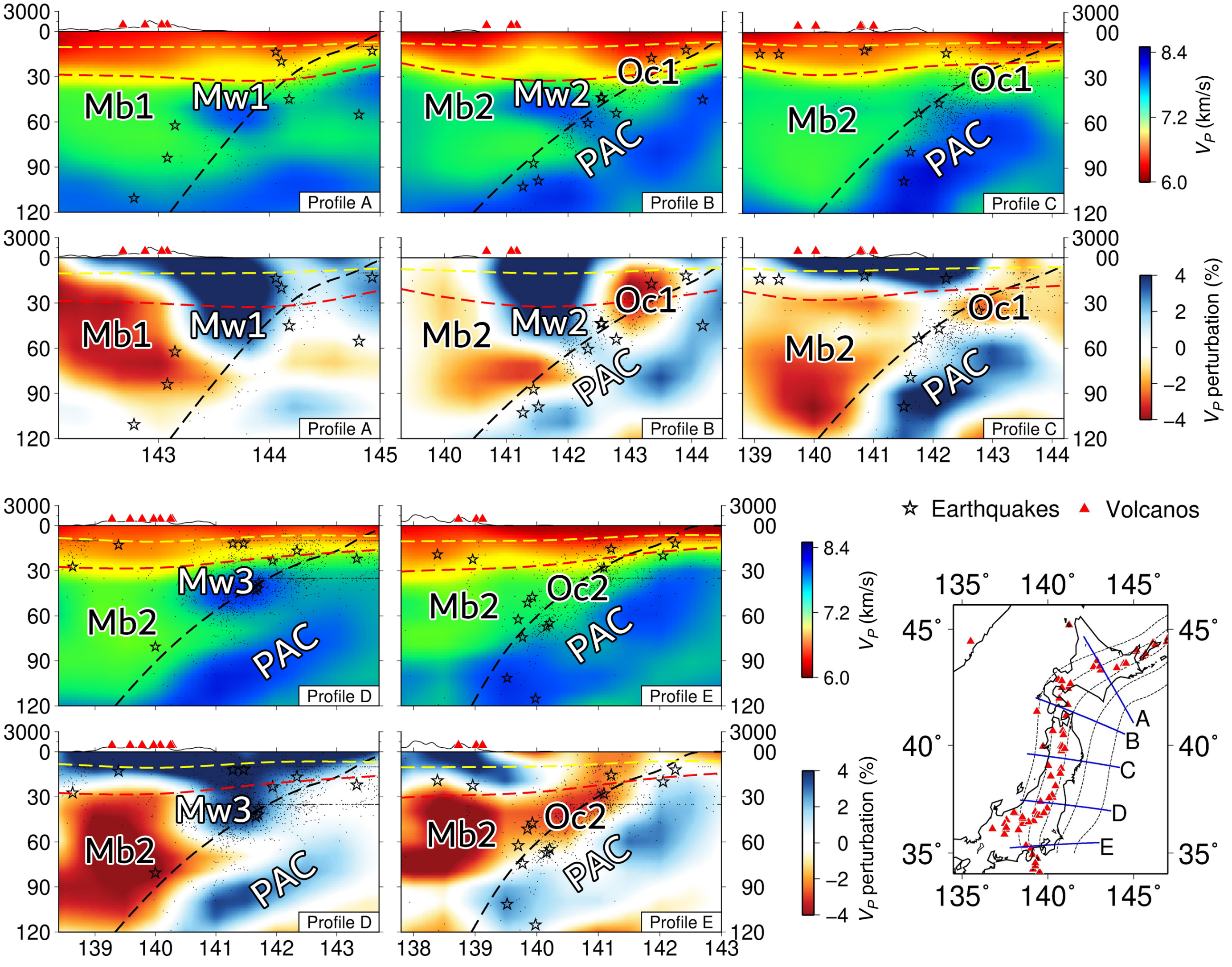

Figure 8. Vertical profiles of the inversion result for which the locations are denoted by blue lines in the right bottom figure. The absolute V_P model and the V_P perturbation model with respect to the 3D initial model are aligned. Prominent low- and high-velocity anomalies are labeled in each profile (PAC: the Pacific Plate; Mb1 and Mb2: magma body; Mw1–Mw3: mantle wedge; Oc1 and Oc2: oceanic crust). The stars represent the earthquakes used in the inversion within 50 km along the profile. And small black dots are the earthquakes with magnitudes larger than 1.5 since 2004. The topography is plotted on the top coupled with major volcanoes represented by red triangles. The yellow and red dashed lines are Conrad and Moho discontinuities from CRUST1.0 (Laske *et al.*, 2013). The upper boundary of the subducting Pacific slab is denoted by black dashed lines obtained from Slab2.0 (Hayes *et al.*, 2018). The color version of this figure is available only in the electronic edition.

between these models. Thus, we believe that the labeled velocity anomalies in the tomographic images are reliable features rather than artifacts.

Discussion

Subducting slab

Northeastern Japan sits on a typical subduction zone, in which the Pacific slab is subducting northwestward along the Kuril–Japan trench. This subduction process dominates the geological dynamics in this area, leading to intense volcanic and seismic activities as well as mantle magmatism. As a significant feature, the subducting Pacific slab is illuminated as a landward dipping high-velocity body by many large-scale seismic studies (e.g., Friederich, 2003; Gorbatov and Kennett, 2003; Huang and Zhao, 2006; Koulakov, 2011; Obayashi *et al.*, 2013; Chen *et al.*, 2015; Wei *et al.*, 2015) and confirmed by regional and local attenuation tomography (e.g., Liu *et al.*, 2014; Wang *et al.*, 2017; Wang and Zhao, 2019; Yu and Zhao, 2020). The Pacific slab is much colder than the surrounding mantle (Honda, 1985; Ji *et al.*, 2017) and exhibits as a high-V and high-Q zone in tomographic images, similar to other subducting slabs, for example, the ones in the Sumatra subduction zone (Liu *et al.*, 2021) and the central Andes subduction zone (Gao *et al.*, 2021).

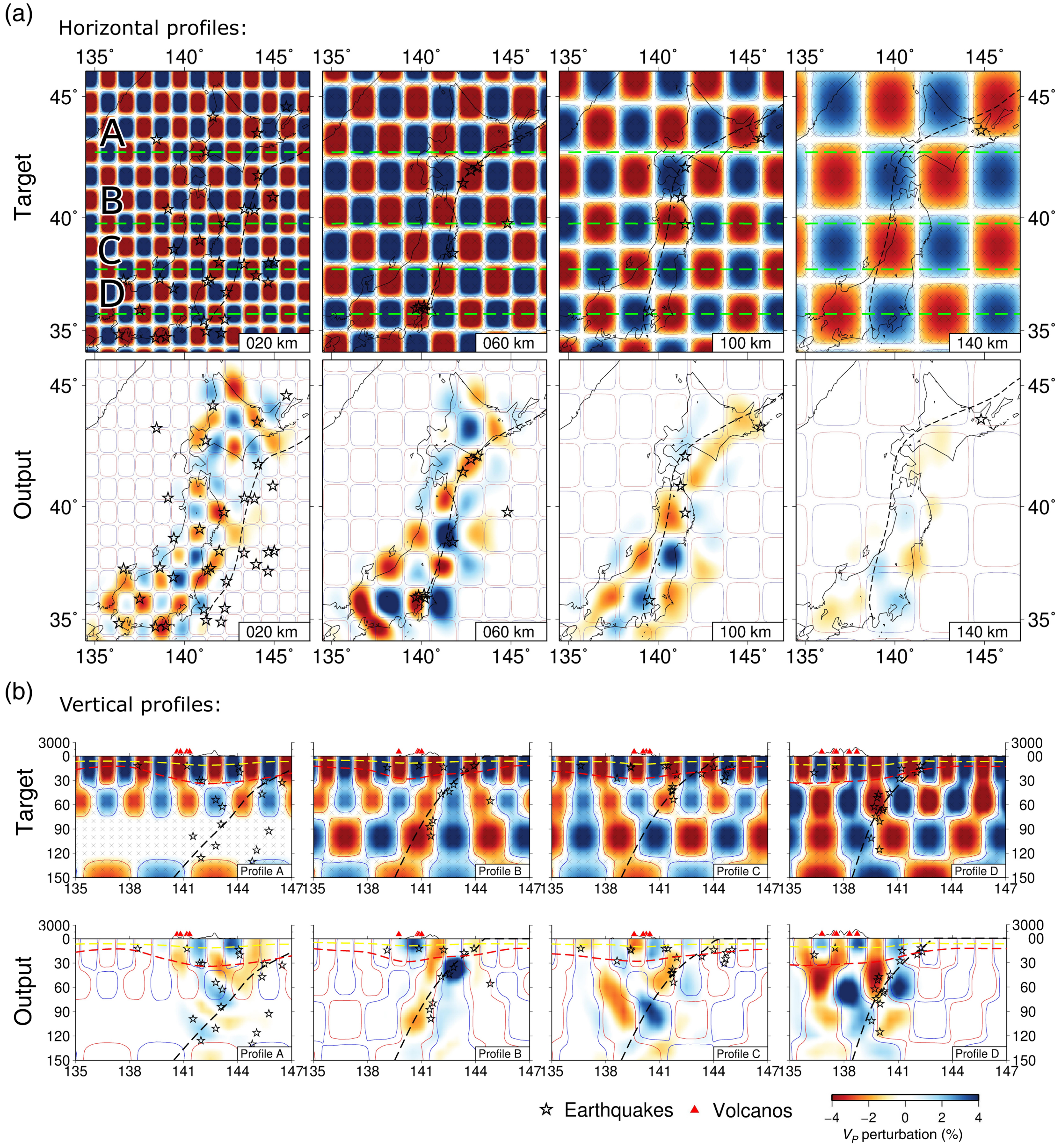

Figure 9. The V_P perturbation of the checkerboard target model and the output model. (a) Top: horizontal profiles of the checkerboard target model at different depths; bottom: horizontal profiles of the output model at different depths. (b) Top: vertical profiles of the checkerboard target model for which the locations are indicated as green dashed lines in horizontal profiles; bottom: vertical profiles of the output model. The yellow, red, and black dashed lines represent the Conrad, Moho discontinuity interface and the upper boundary of the Pacific plate, respectively. Earthquakes are denoted by black stars. The color version of this figure is available only in the electronic edition.

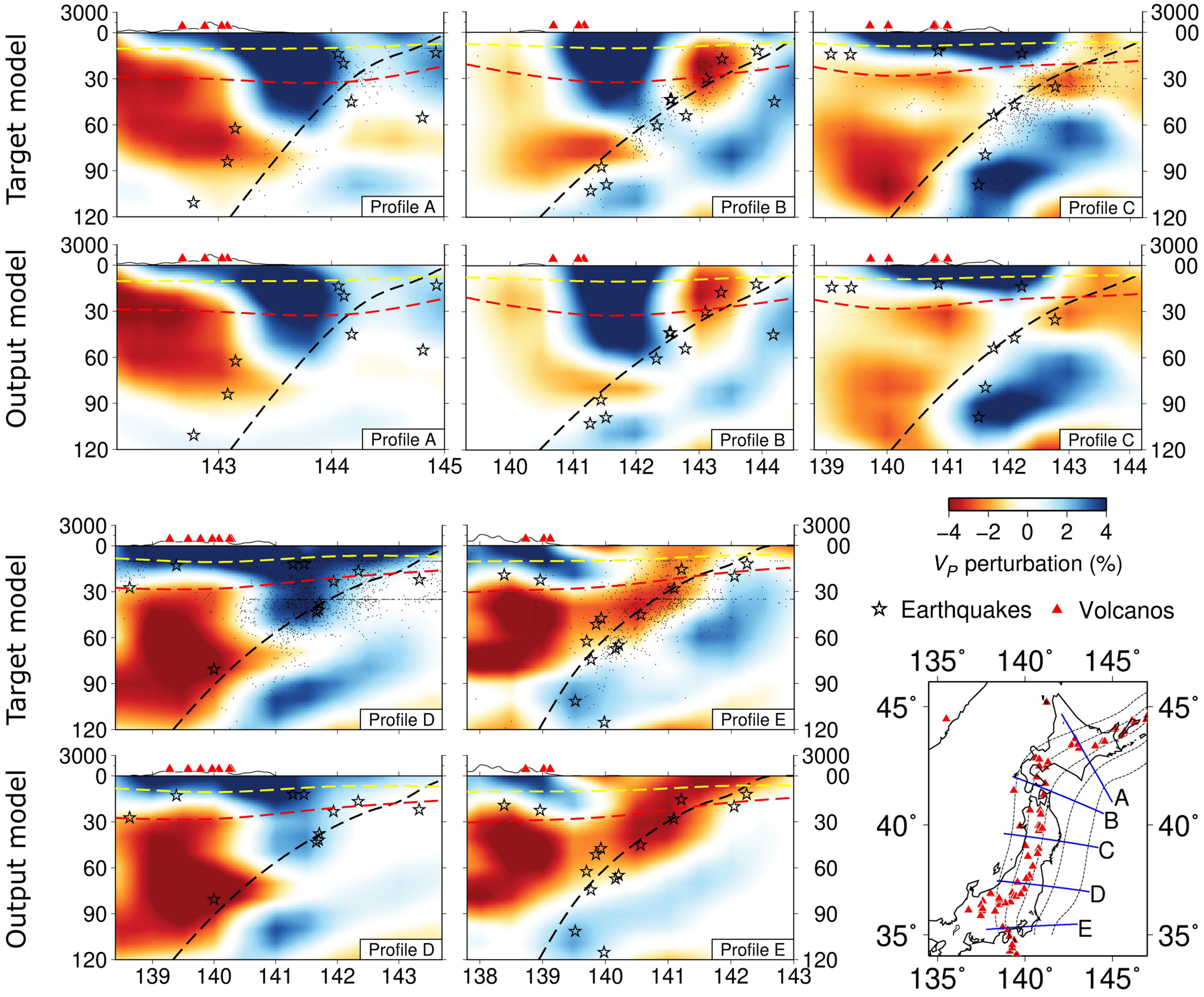

Figure 10. The V_P perturbation of the output model for the restoring resolution test. Both the output model and target model at vertical profiles are aligned for comparison. All symbols are the same as in Figure 8. The color version of this figure is available only in the electronic edition.

In our study region down to 120 km depth, the Pacific subducting slab is imaged as a landward dipping high-velocity zone (Fig. 7, PAC). As shown in the horizontal profiles in Figure 7, the high-V_P body PAC fits well with the upper boundary of the Pacific subducting slab from Slab2.0 (Hayes *et al.*, 2018) and also coincides with the Benioff seismicity (Fig. 8, small black dots). Both the checkerboard and restoring resolution tests verify the robustness and reliability of the high-V_P anomaly PAC. Because of the lack of data coverage, the region deeper than 90 km beneath Hokkaido is not well resolved, where the high V_P anomaly PAC terminates (Fig. 8, profile A). It is also reflected by the checkerboard test, which shows a smearing at 100 km depth in the northeast (Fig. 9a).

Some previous studies that focus on the subducting zone beneath Japan assign a dipping high-velocity anomaly to the initial model (e.g., Zhao *et al.*, 2012; Simutė *et al.*, 2016; Yu and Zhao, 2020). The reason is that the geometry of the subducting slab is well determined, for example, by Slab2.0 (Hayes *et al.*, 2018). This prior information sometimes is helpful to constrain the subsurface structure atop the slab. However, we choose to perform the inversion from a carefully constructed 3D initial model with no prior information about the subducting slab. Nonetheless, an apparent dipping high-V_P anomaly PAC is illuminated as the Pacific subducting slab, and its upper boundary is consistent with the findings of other studies. This feature indicates that the subduction slab is resolvable using the common-source double-difference travel-time adjoint tomography method, even only with about 100 earthquakes.

Low-V_P body beneath the volcanic arc

Our tomographic result contains low-velocity zones (Mb1 and Mb2) beneath the volcanic arc and back-arc in Hokkaido and Tohoku, which exist in the crust and mantle wedge above the subducting slab (see Figs. 7 and 8). However, there are positive V_P perturbations from the 3D initial model above Mb1 and Mb2 at 10 km depth (Fig. 8, profiles A–E; Fig. S1, 10 km). Actually, the absolute V_P value beneath the volcanic arc is still lower than the surrounding. The reliability of these low-V_P bodies is also verified by both the checkerboard and restoring resolution tests. These low-V_P bodies may reflect the arc magmatism triggered by the subduction process beneath northeastern Japan. Abundant water content in the Pacific oceanic crust is dragged down by subduction. With the temperature and pressure increase, fluids are released from the subducting slab due to the breaking down of hydrous minerals. Then, the addition of water lowers the solidus temperature of peridotites and induces hydrous melting in the overlying mantle (Tatsumi, 1986), resulting in low-V_P zones in the mantle wedge.

Recent studies focusing on the Japan Islands have presented similar tomographic results, showing low-V and low-Q zones in the mantle wedge beneath the volcanic arc (e.g., Zhao *et al.*, 2012; Liu *et al.*, 2014; Liu and Zhao, 2016; Simutė *et al.*, 2016; Wang *et al.*, 2017; Wang and Zhao, 2019; Yu and Zhao, 2020). As a typical characteristic in the subduction zone, this low-V and low-Q body in the mantle wedge beneath the back-arc and volcano arc is not only detected in northeastern Japan, but also illuminated in other subduction zones all over the world, such as Tonga (Wei *et al.*, 2016), western central Andes (Gao *et al.*, 2021), New Zealand (Eberhart-Phillips *et al.*, 2008), and Alaska (Martin-Short *et al.*, 2018). Our inversion result shows high consistency with the tomographic images mentioned earlier, verifying the effectiveness and robustness of the wave equation-based common-source double-difference travel-time adjoint tomography method to image subduction zones.

Cold and dry fore-arc mantle wedge

We observe strong lateral velocity variations in the mantle wedge at 30–60 km depths. Along the subduction direction from east to west, high-velocity anomalies Mw1–Mw3 in the fore-arc mantle wedge transform to low-velocity bodies Mb1 and Mb2 beneath the volcanic arc and back-arc (Fig. 8). There might be two reasons accounting for the velocity-unreduced fore-arc mantle wedge: the low temperature and few water content. First, compared to the high-heat flows (>80 mW/m^2) at the volcanic arc, the heat flows in the fore-arc region steeply decrease to 30–40 mW/m^2 (Furukawa, 1993; Tanaka *et al.*, 2004), which may contribute to the lateral V_P variation in the mantle wedge. Besides, the surface heat flow of 30–40 mW/m^2 in the fore-arc region implies a temperature of less than 400°C and a V_P greater than 8.2 km/s (Hyndman and Peacock, 2003), which is well consistent with the high-velocity anomalies (Mw1–Mw3) imaged in this study. Second, the low degree of serpentinization is another factor causing the high-V_P anomaly in the fore-arc mantle wedge, which is closely connected to the water content. According to the low ^{3}He/^{4}He ratio from the gas sample observed in the fore-arc region of Hokkaido and Tohoku (Sano and Wakita, 1988), a low degree of serpentinization in the fore-arc mantle wedge is inferred (Umeda *et al.*, 2007). It may arise from the insufficient water content interacting with the mantle rocks. In northeast Japan, a relatively cold subduction zone, the decoupling plate interface terminates at about 70 km depth (Furukawa, 1993). It means that the dehydration process is too slow to hydrate the entire fore-arc mantle above 80 km (Abers *et al.*, 2017), and thus, a small amount of water is released to the fore-arc mantle wedge. As a result, rocks in the fore-arc mantle wedge with a low degree of serpentinization are imaged as high-velocity anomalies Mw1–Mw3. Besides, low-velocity zones Oc1 and Oc2 are interpreted as the hydrous oceanic crust on the upper boundary of the Pacific subducting slab. These features have been confirmed by the restoring resolution test, which also show high consistency with previous tomographic results (Matsubara *et al.*, 2005; Yu and Zhao, 2020). Thus, we believe the fore-arc mantle wedge in northeast Japan is cold and dry.

In many previous studies focusing on northeast Japan, the high-velocity anomaly in the fore-arc mantle wedge is not evident due to the lack of data coverage (e.g., Huang *et al.*, 2011; Laske *et al.*, 2013). Thanks to the waveform data recorded by the newly operated S-net, the dry and cold fore-arc mantle wedge is clearly revealed as high-velocity anomalies in our inversion result and some recent tomographic images (e.g., Yu and Zhao, 2020), which coincides with the high-Q anomaly in the attenuation tomography (e.g., Tsumura *et al.*, 2000; Liu *et al.*, 2014; Wang *et al.*, 2017; Wang and Zhao, 2019). Cold and dry fore-arc mantle wedges may also exist in other subduction zones, for example, the central Andes subduction zone (Gao *et al.*, 2021) and the Hikurangi subduction zone (Eberhart-Phillips *et al.*, 2008). These tomographic images show similar tectonic features as our inversion result.

Conclusion

We have performed the wave equation-based adjoint tomography to image the crust and uppermost mantle beneath northeast Japan using the P-wave common-source double-difference travel times. Compared to traditional methods, this new double-difference travel-time approach is insensitive to the uncertainties of the source-term and source-side structure, which is more likely to reveal robust tectonic features in subduction zones.

According to the tomographic images, the landward-dipping Pacific subducting slab is revealed as a high-V_P anomaly, and its geometry fits well with Slab2.0 and the Benioff seismicity. In the volcanic arc region, low-velocity anomalies are observed in the crust and uppermost mantle above the subducting slab. This anomaly is closely related to the arc magmatism that triggers volcanism in northeast Japan. Thanks to the newly deployed S-net, high-velocity bodies and low-velocity layers atop the subducting slab in the fore-arc region are clearly imaged. These features may reflect the cold and dry fore-arc mantle wedge and hydrous oceanic crust, resulting from the low temperature and the deeper termination depth of the decoupling plate interface in this cold subduction zone. These features are consistent with the previous studies, and their reliability is also confirmed by the checkerboard and restoring resolution tests. Thus, we conclude that the wave equation-based common-source double-difference travel-time adjoint tomography method is an effective and robust technique to image crust and uppermost mantle structures.

Data and Resources

Earthquake information can be accessed from https://www.globalcmt.org/CMTsearch.html. Continuous waveform data of High Sensitivity Seismograph Network (Hi-net) and Seafloor Observation Network (S-net) are available from https://www.hinet.bosai.go.jp and https://www.seafloor.bosai.go.jp, respectively. All the websites were last accessed in March 2022. The supplemental material includes four additional figures.

Declaration of Competing Interests

The authors acknowledge that there are no conflicts of interest recorded.

Acknowledgments

This work is supported by the Minister of Education, Singapore, under its MOE AcRF Tier-2 Grant (04MNP002073C230). This work is also supported by the National Natural Science Foundation of China (Grant Numbers 11871297 and U1839206), the National Key Research and Development Program of China on Monitoring, Early Warning and Prevention of Major Natural Disaster (Grant Number 2017YFC1500301), and Tsinghua University Initiative Scientific Research Program. The authors are grateful for National Research Institute for Earth Science and Disaster Resilience (NIED) to provide continuous seismograms recorded by High Sensitivity Seismograph Network (Hi-net) and Seafloor Observation Network (S-net). The authors thank Allison Bent, Brandon Schmandt, Andreas Fichtner, and an anonymous reviewer for their constructive suggestions and remarkable comments, which are helpful to improve this article.

References

Abers, G. A., P. E. Van Keken, and B. R. Hacker (2017). The cold and relatively dry nature of mantle forearcs in subduction zones, *Nature Geosci.* **10,** 333–337.

Aki, K., and W. H. K. Lee (1976). Determination of three-dimensional velocity anomalies under a seismic array using first P arrival times from local earthquakes: 1. A homogeneous initial model, *J. Geophys. Res.* **81,** no. 23, 4381–4399.

Baig, A. M., F. A. Dahlen, and S.-H. Hung (2003). Travel times of waves in three-dimensional random media, *Geophys. J. Int.* **153,** no. 2, 467–482.

Bamberger, A., G. Chavent, C. Hemons, and P. Lailly (1982). Inversion of normal incidence seismograms, *Geophysics* **47,** 757–770.

Bird, P. (2003). An updated digital model of plate boundaries, *Geochem. Geophys. Geosys.* **4,** no. 3, doi: 10.1029/2001GC000252.

Brune, J., and J. Dorman (1963). Seismic waves and earth structure in the Canadian shield, *Bull. Seismol. Soc. Am.* **53,** no. 1, 167–210.

Chen, J., S.-K. Kufner, X. Yuan, B. Heit, H. Wu, D. Yang, B. Schurr, and S. Kay (2020). Lithospheric delamination beneath the southern Puna plateau resolved by local earthquake tomography, *J. Geophys. Res.* **125,** no. 10, e2019JB019040, doi: 10.1029/2019JB019040.

Chen, M., F. Niu, Q. Liu, J. Tromp, and X. Zheng (2015). Multiparameter adjoint tomography of the crust and upper mantle beneath east Asia: 1. Model construction and comparisons, *J. Geophys. Res.* **120,** 1762–1786.

Chen, P., L. Zhao, and T. H. Jordan (2007). Full 3D tomography for the crustal structure of the Los Angeles region, *Bull. Seismol. Soc. Am.* **97,** 1094–1120.

Dahlen, F. A., S.-H. Hung, and G. Nolet (2000). Fréchet kernels for finite-frequency traveltime—I. Theory, *Geophys. J. Int.* **141,** 157–174.

de Vos, D., H. Paulssen, and A. Fichtner (2013). Finite-frequency sensitivity kernels for two-station surface wave measurements, *Geophys. J. Int.* **194,** 1042–1049.

Eberhart-Phillips, D., M. Reyners, M. Chadwick, and G. Stuart (2008). Three-dimensional attenuation structure of the Hikurangi subduction zone in the central North Island, New Zealand, *Geophys. J. Int.* **174,** no. 1, 418–434.

Evans, J. R., D. Eberhart-Phillips, and C. H. Thurber (1994). User's manual for SIMULPS12 for imaging Vp and Vp/Vs; a derivative of the "Thurber" tomographic inversion SIMUL3 for local earthquakes and explosions, *U.S. Geol. Surv. Open-File Rept. (94-431)*, doi: 10.3133/ofr94431.

Fang, H., and H. Zhang (2014). Wavelet-based double-difference seismic tomography with sparsity regularization, *Geophys. J. Int.* **199,** no. 2, 944–955.

Fichtner, A., H.-P. Bunge, and H. Igel (2006). The adjoint method in seismology I. Theory, *Phys. Earth Planet. In.* **157,** 86–104.

Fichtner, A., H. Igel, H.-P. Bunge, and B. L. N. Kennett (2009). Simulation and inversion of seismic wave propagation on continental scales based on a spectral-element method, *J. Numer. Anal. Ind. Appl. Math.* **4,** 11–22.

Fichtner, A., B. L. N. Kennett, H. Igel, and H.-P. Bunge (2009). Full seismic waveform tomography for upper-mantle structure in the Australasian region using adjoint methods, *Geophys. J. Int.* **179,** 1703–1725.

Fremont, M.-J., and S. D. Malone (1987). High precision relative locations of earthquakes at Mount St. Helens, Washington, *J. Geophys. Res.* **92,** 10,223–10,236.

Friederich, W. (2003). The S-velocity structure of the east Asian mantle from inversion of shear and surface waveforms, *Geophys. J. Int.* **153,** 88–102.

Furukawa, Y. (1993). Depth of the decoupling plate interface and thermal structure under arcs, *J. Geophys. Res.* **98,** no. B11, 20,005–20,013.

Gao, Y., F. Tilmann, D.-P. van Herwaarden, S. Thrastarson, A. Fichtner, B. Heit, X. Yuan, and B. Schurr (2021). Full waveform inversion beneath the central Andes: Insight into the dehydration of the Nazca slab and delamination of the back-arc lithosphere, *J. Geophys. Res.* **126,** e2021JB021984, doi: 10.1029/2021JB021984.

Gokhberg, A., and A. Fichtner (2016). Full-waveform inversion on heterogeneous HPC systems, *Comput. Geosci.* **89,** 260–268.

Goldstein, P., and A. Snoke (2005). SAC availability for the IRIS community, *Incorporated Institutions for Seismology Data Management Center* Electronic Newsletter, available at https://www.osti.gov/biblio/875360 (last accessed March 2022).

Gorbatov, A., and B. Kennett (2003). Joint bulk-sound and shear tomography for western Pacific subduction zones, *Earth Planet. Sci. Lett.* **210,** 527–543.

Got, J.-L., J. Fréchet, and F. W. Klein (1994). Deep fault plane geometry inferred from multiplet relative relocation beneath the south flank of Kilauea, *J. Geophys. Res.* **99,** no. B8, 15,375–15,386.

Hayes, G. P., G. L. Moore, D. E. Portner, M. Hearne, H. Flamme, M. Furtney, and G. M. Smoczyk (2018). Slab2, a comprehensive subduction zone geometry model, *Science* **362,** 58–61.

Hirose, F., J. Nakajima, and A. Hasegawa (2008). Three-dimensional seismic velocity structure and configuration of the Philippine Sea slab in southwestern Japan estimated by double-difference tomography, *J. Geophys. Res.* **113,** no. B9, doi: 10.1029/2007jb005274.

Honda, S. (1985). Thermal structure beneath Tohoku, northeast Japan, *Tectonophysics* **112,** no. 1, 69–102.

Huang, J., and D. Zhao (2006). High-resolution mantle tomography of China and surrounding regions, *J. Geophys. Res.* **111,** doi: 10.1029/2005JB004066.

Huang, Z., D. Zhao, and L. Wang (2011). Seismic heterogeneity and anisotropy of the Honshu arc from the Japan trench to the Japan sea, *Geophys. J. Int.* **184,** 1428–1444.

Humphreys, E., and R. W. Clayton (1988). Adaption of back projection tomography to seismic travel time problems, *J. Geophys. Res.* **93,** 1073–1085.

Hung, S.-H., F. A. Dahlen, and G. Nolet (2001). Wavefront healing: A banana–doughnut perspective, *Geophys. J. Int.* **146,** 289–312.

Hyndman, R. D., and S. M. Peacock (2003). Serpentinization of the forearc mantle, *Earth Planet. Sci. Lett.* **212,** nos. 3/4, 417–432.

Igel, H., H. Djikpesse, and A. Tarantola (1996). Waveform inversion of marine reflection seismograms for P-impedance and Poisson's ratio, *Geophys. J. Int.* **124,** 363–371.

Ji, Y., S. Yoshioka, V. C. Manea, M. Manea, and T. Matsumoto (2017). Three-dimensional numerical modeling of thermal regime and slab dehydration beneath Kanto and Tohoku, Japan, *J. Geophys. Res.* **122,** 332–353.

Kanazawa, T. (2013). Japan trench earthquake and tsunami monitoring network of cable-linked 150 ocean bottom observatories and its impact to earth disaster science, *2013 IEEE International Underwater Technology Symposium (UT)*, 1–5, doi: 10.1109/UT.2013.6519911.

Kennett, B. L. N., E. R. Engdahl, and R. Buland (1995). Constraints on seismic velocities in the Earth from travel times, *Geophys. J. Int.* **122,** 108–124.

Kissling, E. (1988). Geotomography with local earthquake data, *Rev. Geophys.* **26,** 659–698.

Kissling, E., W. L. Ellsworth, D. Eberhart-Phillips, and U. Kradolfer (1994). Initial reference models in local earthquake tomography, *J. Geophys. Res.* **99,** 19,635–19,646.

Komatitsch, D. (2011). Fluid–solid coupling on a cluster of GPU graphics cards for seismic wave propagation, *C. R. Mec.* **339,** 125–135.

Komatitsch, D., and J. Tromp (1999). Introduction to the spectral-element method for 3-D seismic wave propagation, *Geophys. J. Int.* **139,** no. 3, 806–822.

Komatitsch, D., and J.-P. Vilotte (1998). The spectral element method: An efficient tool to simulate the seismic response of 2D and 3D geological structures, *Bull. Seismol. Soc. Am.* **88,** 368–392.

Koulakov, I. (2011). High-frequency P and S velocity anomalies in the upper mantle beneath Asia from inversion of worldwide traveltime data, *J. Geophys. Res.* **116,** no. B4, doi: 10.1029/2010JB007938.

Laske, G., G. Masters, Z. Ma, and M. Pasyanos (2013). Update on CRUST1.0—A 1-degree global model of Earth's crust, *Geophys. Res. Abstr.* 15**,** Abstract EGU2013-2658, available at https://meetingorganizer.copernicus.org/EGU2013/EGU2013-2658.pdf (last accessed March 2022).

Liu, Q., and J. Tromp (2006). Finite-frequency kernels based on adjoint methods, *Bull. Seismol. Soc. Am.* **96,** 2383–2397.

Liu, X., and D. Zhao (2016). P and S wave tomography of Japan subduction zone from joint inversions of local and teleseismic travel times and surface-wave data, *Phys. Earth Planet. In.* **252,** 1–22.

Liu, S., I. Suardi, X. Xu, S. Yang, and P. Tong (2021). The geometry of the subducted slab beneath Sumatra revealed by regional and teleseismic traveltime tomography, *J. Geophys. Res.* 126**,** e2020JB020169, doi: 10.1029/2020JB020169.

Liu, X., D. Zhao, and S. Li (2014). Seismic attenuation tomography of the Northeast Japan arc: Insight into the 2011 Tohoku earthquake (Mw 9.0) and subduction dynamics, *J. Geophys. Res.* **119,** 1094–1118.

Marquering, H., F. A. Dahlen, and G. Nolet (1999). Three-dimensional sensitivity kernels for finite-frequency travel times: The banana-doughnut paradox, *Geophys. J. Int.* **137,** 805–815.

Martin-Short, R., R. Allen, I. D. Bastow, R. W. Porritt, and M. S. Miller (2018). Seismic imaging of the Alaska subduction zone: Implications for slab geometry and volcanism, *Geochem. Geophys. Geosys.* **19,** 4541–4560.

Matsubara, M., H. Hayashi, K. Obara, and K. Kasahara (2005). Low-velocity oceanic crust at the top of the Philippine Sea and Pacific plates beneath the Kanto region, central Japan, imaged by seismic tomography, *J. Geophys. Res.* **110,** no. B12, doi: 10.1029/2005JB003673.

Obayashi, M., J. Yoshimitsu, G. Nolet, Y. Fukao, H. Shiobara, H. Sugioka, H. Miyamachi, and Y. Gao (2013). Finite frequency whole mantle P wave tomography: Improvement of subducted slab images, *Geophys. Res. Lett.* **40,** 5652–5657.

Okada, Y., K. Kasahara, S. Hori, K. Obara, S. Sekiguchi, H. Fujiwara, and A. Yamamoto (2004). Recent progress of seismic observation networks in Japan: Hi-net, F-net, K-net and KiK-net, *Earth Planets Space* **56,** 15–28.

Örsvuran, R., E. Bozdağ, R. Modrak, W. Lei, and Y. Ruan (2020). Double-difference measurements in global full-waveform inversions, *Geophys. J. Int.* **220,** 661–680.

Poupinet, G., W. L. Ellsworth, and J. Fréchet (1984). Monitoring velocity variations in the crust using earthquake doublets: An application to the Calaveras fault, California, *J. Geophys. Res.* **89,** no. B7, 5719–5731.

Pratt, R. G. (1999). Seismic waveform inversion in the frequency domain. Part 1: Theory and verification in a physical scale model, *Geophysics* **64,** 888–901.

Rawlinson, N., S. Pozgay, and S. Fishwick (2010). Seismic tomography: A window into deep Earth, *Phys. Earth Planet. In.* **178,** 101–135.

Richards-Dinger, K. B., and P. M. Shearer (2000). Earthquake locations in southern California obtained using source specific station terms, *J. Geophys. Res.* **105,** no. B5, 10,939–10,960.

Sano, Y., and H. Wakita (1988). Helium isotope ratio and heat discharge rate in the Hokkaido Island, northeast Japan, *Geochem. J.* **22,** no. 6, 293–303.

Simutė, S., H. Steptoe, L. Cobden, A. Gokhberg, and A. Fichtner (2016) Full-waveform inversion of the Japanese Islands region, *J. Geophys. Res.* **121,** 3722–3741.

Sippl, C., B. Schurr, G. Asch, and J. Kummerow (2018). Seismicity structure of the northern Chile forearc from >100,000 double-difference relocated hypocenters, *J. Geophys. Res.* **123,** no. 5, 4063–4087.

Takagi, R., N. Uchida, T. Nakayama, R. Azuma, A. Ishigami, T. Okada, T. Nakamura, and K. Shiomi (2019). Estimation of the orientations of the S-net cabled ocean-bottom sensors, *Seismol. Res. Lett.* **90,** no. 6, 2175–2187.

Tanaka, A., M. Yamano, Y. Yano, and M. Sasada (2004). Geothermal gradient and heat flow data in and around Japan (I): Appraisal of heat flow from geothermal gradient data, *Earth Planets Space* **56,** no. 12, 1191–1194.

Tape, C., Q. Liu, A. Maggi, and J. Tromp (2009). Adjoint tomography of the southern California crust, *Science* **325,** 988–992.

Tape, C., Q. Liu, A. Maggi, and J. Tromp (2010). Seismic tomography of the southern California crust based on spectral-element and adjoint methods, *Geophys. J. Int.* **180,** 433–462.

Tarantola, A. (1984). Inversion of seismic reflection data in the acoustic approximation, *Geophysics* **49,** 1259–1266.

Tatsumi, Y. (1986). Formation of the volcanic front in subduction zones, *Geophys. Res. Lett.* **13,** no. 8, 717–720.

Thurber, C. H. (1983). Earthquake locations and three-dimensional crustal structure in the Coyote lake area, central California, *J. Geophys. Res.* **88,** no. B10, 8226–8236.

Tong, P. (2021). Adjoint-state travel time tomography: Eikonal equation-based methods and application to the Anza area in southern California, *J. Geophys. Res.* 126**,** e2021JB021818, doi: 10.1029/2021JB021818.

Tromp, J. (2020). Seismic wavefield imaging of Earth's interior across scales, *Nat. Rev. Earth Environ.* **1,** 40–53.

Tromp, J., C. Tape, and Q. Liu (2005). Seismic tomography, adjoint methods, time reversal and banana doughnut kernels, *Geophys. J. Int.* **160,** no. 1, 195–216.

Tsumura, N., S. Matsumoto, S. Horiuchi, and A. Hasegawa (2000). Three-dimensional attenuation structure beneath the northeastern Japan arc estimated from spectra of small earthquakes, *Tectonophysics* **319,** no. 4, 241–260.

Umeda, K., G. F. McCrank, and A. Ninomiya (2007). Helium isotopes as geochemical indicators of a serpentinized fore-arc mantle wedge, *J. Geophys. Res.* **112,** no. B10, doi: 10.1029/2007JB005031.

van der Hilst, R. D., S. Widiyantoro, and E. R. Engdahl (1997). Evidence for deep mantle circulation from global tomography, *Nature* **386,** 578–584.

VanDecar, J. C., and R. S. Crosson (1990). Determination of teleseismic relative phase arrival times using multi-channel cross-correlation and least squares, *Bull. Seismol. Soc. Am.* **80,** no. 1, 150–169.

Waldhauser, F., and W. L. Ellsworth (2000). A double-difference earthquake location algorithm: Method and application to the northern Hayward fault, California, *Bull. Seismol. Soc. Am.* **90,** no. 6, 1353–1368.

Wang, Z. W., and D. Zhao (2019). Updated attenuation tomography of Japan subduction zone, *Geophys. J. Int.* **219,** no. 3, 1679–1697.

Wang, Z. W., D. Zhao, X. Liu, C. Chen, and X. Li (2017). P and S wave attenuation tomography of the Japan subduction zone, *Geochem. Geophys. Geosys.* **18,** 1688–1710.

Wei, S. S., Y. Zha, W. Shen, D. A. Wiens, J. A. Conder, and S. C. Webb (2016). Upper mantle structure of the Tonga-Lau-Fiji region from Rayleigh wave tomography, *Geochem. Geophys. Geosys.* **17,** 4705–4724.

Wei, W., D. Zhao, J. Xu, F. Wei, and G. Liu (2015). P and S wave tomography and anisotropy in northwest Pacific and east Asia: Constraints on stagnant slab and intraplate volcanism, *J. Geophys. Res.* **120,** 1642–1666.

Woodward, M. J. (1992). Wave-equation tomography, *Geophysics* **57,** no. 1, 15–26.

Yoshizawa, K., and B. L. N. Kennett (2004). Multimode surface wave tomography for the Australian region using a three-stage approach incorporating finite frequency effects, *J. Geophys. Res.* **109,** no. B2, doi: 10.1029/2002JB002254.

Yu, Z., and D. Zhao (2020). Seismic evidence for water transportation in the forearc off northern Japan, *J. Geophys. Res.* **125,** doi: 10.1029/2019JB018600.

Yuan, Y. O., F. J. Simons, and J. Tromp (2016). Double-difference adjoint seismic tomography, *Geophys. J. Int.* **206,** 1599–1618.

Zhang, H., and C. H. Thurber (2003). Double-difference tomography: The method and its application to the Hayward fault, California, *Bull. Seismol. Soc. Am.* **93,** no. 5, 1875–1889.

Zhang, H., C. H. Thurber, D. Shelly, S. Ide, G. C. Beroza, and A. Hasegawa (2004). High-resolution subducting-slab structure beneath northern Honshu, Japan, revealed by double-difference tomography, *Geology* **32,** no. 4, 361–364.

Zhao, D. (2015). The 2011 Tohoku earthquake (Mw 9.0) sequence and subduction dynamics in western Pacific and east Asia, *J. Asian Earth Sci.* **98,** 26–49.

Zhao, D., A. Hasegawa, and S. Horiuchi (1992). Tomographic imaging of P and S wave velocity structure beneath northeastern Japan, *J. Geophys. Res.* **97,** no. B13, 19,909–19,928.

Zhao, D., T. Yanada, A. Hasegawa, N. Umino, and W. Wei (2012). Imaging the subducting slabs and mantle upwelling under the Japan Islands, *Geophys. J. Int.* **190,** no. 2, 816–828.

Zhou, Y., F. A. Dahlen, G. Nolet, and G. Laske (2005). Finite-frequency effects in global surface-wave tomography, *Geophys. J. Int.* **163,** 1087–1111.

Manuscript received 2 November 2021
Published online 16 March 2022